High Q Antisymmetric Mode Lithium Niobate MEMS Resonators With Spurious Mitigation

Yansong Yang, *Member, IEEE*, Ruochen Lu, *Member, IEEE*, and Songbin Gong, *Senior Member, IEEE*

***Abstract*— This paper reports on the demonstrations of first-order antisymmetric Lamb wave (A1) mode resonator as a new platform for front-end filtering of the fifth-generation (5G) wireless communication. The sub-6 GHz resonance in this work is achieved by employing the A1 mode in the micromachined Y-cut Lithium Niobate ($LiNbO_3$) thin films. The spurious modes mitigation is achieved by optimizing the distribution of the electric field. The demonstrated figure-of-merit (FoM = $Q \cdot k_t^2$) of 435 marks the first time that a new resonator technology with the FoMs exceeds those of surface acoustic wave (SAW) resonators and thin-film bulk acoustic resonators (FBARs) in the sub-6 GHz (1-6 GHz) frequency range. [2019-0241]**

***Index Terms*— 5G, IoT, Sub-6 GHz, acoustic resonator, lithium niobate, MEMS, spurious suppression.**

I. Introduction

IN RESPONSE to customers' demand for more mobile video streaming, cloud computing, virtual reality, and Internet-of-Things (IoT) applications, the global mobile data traffic is projected to increase by 45% per year in the next decade [1]–[3]. To keep up with the explosion of data, wireless providers around the globe plan to resort to the fifth-generation (5G) for overcoming the limitations of existing wireless networks (4G). In contrast to 4G, 5G will involve significantly expanded capacity via accessing larger physical bandwidths and deploying new technologies capable of such. To attain the large physical bandwidths while co-existing with incumbent wireless applications, 5G networks will take on either an unallocated spectrum at beyond 4G frequencies or spectrum that can be repurposed. Recent releases from various wireless standardization organizations (e.g., 3GPP) have shown the spectrum allocations around the world converging to either the sub-6 GHz spectrum where physical bandwidths are ranging from 20 MHz to 600 MHz, or the millimeter-wave (mm-wave) spectrum (several bands in Ka-band) where close to 1 GHz bandwidths are accessible [4], [5]. While the millimeter-wave frequencies are certainly less crowded and are more available, various outstanding challenges (e.g., spatial filtering, and power efficiency) have to be addressed before they are ready for prime time. These technological challenges associated with mm-wave imply that mobile operators are likely to rely heavily on the sub-6 GHz spectrum for the initial 5G deployment and certain mission-critical applications for its high reliability and low latency.

Although the sub-6 GHz systems are considered less difficult because their front-ends are likely to feature a similar architecture to LTE systems and several front-end building blocks can be readily scaled up in frequency from their 4G counterparts, they are not without their own challenges. One key challenge arises from the significant increase in fractional bandwidths (FBW) transitioning from 4G to 5G. LTE bands, which have physical bandwidths ranging from 3 to 20 MHz at a center frequency from 0.4 to 3.7 GHz, have FBW less than 4% [6], [7]. On the other hand, 5G bands can end up demanding an FBW as high as 24% (e.g., 3.3 GHz – 4.2 GHz) [4]. Such a large FBW greatly challenges the capabilities of the incumbent mobile front-end filtering solution, which remains essential for accessing the radio frequency (RF) spectrum and 5G new radio (NR)'s coexistence with current and emerging applications that are spectrally nearby.

The FBW of an acoustic filter is fundamentally set by the electromechanical coupling (k_t^2) of the resonators in the filter. k_t^2 measures the efficiency of electromechanical transduction, which limits the FBW similarly to the inter-resonator coupling limiting the FBWof a filter consisting of inter-coupled resonators. Considering the commonly used ladder filter topology, its maximum FBW is limited by the spectral separation between the series and parallel resonances of the comprising resonators, which is determined by the k_t^2 [8]:

$$FBW \approx \sqrt{(12/\pi^2)k_t^2 + 1} - 1 \quad (1)$$

Currently, surface acoustic wave (SAW) resonators and aluminum nitride (AlN) thin-film bulk acoustic resonators (FBARs) are the commercial solutions for front-end filters and multiplexers. SAW devices, which typically operate below 3 GHz, are challenging to be scaled up in frequency without scarifying performance [9]–[12]. In addition, their k_t^2 is typically around 8%, which implies an FBW of less than 4.7% based on Eq. 1. AlN FBARs, despite having been demonstrated with high Q at all sub-6GHz frequencies, are fundamentally limited in k_t^2 by the piezoelectric coefficients of sputtered polycrystalline AlN [13]–[15]. Although k_t^2 can be enhanced with Sc-doped AlN films [16], [17], the enhancement comes at the cost of much-reduced Q (possibly due to

Manuscript received November 18, 2019; revised December 25, 2019; accepted January 14, 2020. Date of publication February 4, 2020; date of current version April 2, 2020. This work was supported by the DARPA MTO SPAR program. Subject Editor R. N. Candler. *(Corresponding author: Yansong Yang.)*

The authors are with the Department of Electrical and Computing Engineering, University of Illinois at Urbana–Champaign, Urbana, IL 61801 USA (e-mail: yyang165@illinois.edu).

Color versions of one or more of the figures in this article are available online at http://ieeexplore.ieee.org.

Digital Object Identifier 10.1109/JMEMS.2020.2967784

the inclusions induced by dopants [18], [19]), thus resulting in overall degradation in the device figure of merit (FoM $= k_t^2 \cdot Q$) and filter insertion loss (IL). To circumvent the limitations set by k_t^2, other filters topologies that combine reactive elements, lumped [20], distributed [21], or integrated passives device (IPD) [22] with acoustic resonators have been proposed to enlarge the filter BW. These approaches typically resort to an inductive element (or its equivalent) connected in parallel with the acoustic resonator to move the series and anti-resonances of the collective circuit (resonator and inductor) further apart. At sub-1.5 GHz, it requires a large inductance and thus leads to a large filter footprint. At higher frequencies, the inductance is smaller but typically with a lower Q, degrading the IL, out-of-band rejection, and roll-off. Moreover, the final hybrid circuit still requires high k_t^2 devices to meet the very large FBW (e.g. n77-n79) of 5G NR. To simultaneously achieve low IL, large FBW, sharp out-of-band rejection, and steep skirt for 5G filters, acoustic resonators have to be developed with concurrent high k_t^2 and Q, and large FoM up to 6 GHz.

Recently, Lamb wave acoustic or MEMS resonators based on single-crystal X-, Y-, and Z-cut $LiNbO_3$ thin films are receiving increasing research attention and several reported demonstrations have broken the records of FoM due to their high k_t^2 (>20%) and low damping loss [23]–[29]. Despite the demonstrated high FoMs of these Lamb wave mode devices, their moderate phase velocities, 6000 m/s for S0 and 3500 m/s for SH0, make it difficult to cover the entire sub-6 GHz spectrum. To utilize the high piezoelectric coefficients of $LiNbO_3$ material in sub-6 GHz spectrum, the first-order antisymmetric (A1) Lamb-wave mode, which has a very large phase velocity in single-crystal Z-cut $LiNbO_3$ thin films [30], was demonstrated at 5 GHz with a FoM of 153 and $f \cdot Q$ product of 2.3×10^{12}[31]–[33]. In spite of the large FoM in the aforementioned demonstrations, Qs of these devices are still far from the anticipated value of single-crystal $LiNbO_3$ devices at GHz frequencies. Moreover, the spurious modes near the pass-band remain a major bottleneck as they lower k_t^2 of the intended resonance and create in-band ripples and out-of-band spurious responses.

In this study, we exploit the first-order antisymmetric (A1) mode in a transferred Y-cut $LiNbO_3$ thin film with the aim to enhance FoM and $f \cdot Q$, and to suppress the significant spurious modes concurrently. To this end, the resonant frequency, phase velocity, coupling factor, and excitation of the A1 mode are first carefully analyzed. The origins of spurious modes are identified, subsequently leading to their mitigation methods based on electrode design optimization. The final device design feature multiple pairs of electrodes with wide gaps between electrodes to quasi-exclusively harness the piezoelectric transduction for the intended mode. To validate our analysis and modeling, different designs of devices are fabricated on a 1.2 μm thick Y-cut $LiNbO_3$ thin film, and the optimized device is measured with a resonance at 1.65 GHz, a high k_t^2 of 14%, a high Q of 3112, and a near spurious-free response. As listed in Table I, the high FoM demonstrated in our design, which is collectively enabled by high k_t^2 and Q, and the spurious-free response, surpasses state-of-the-art (SOA) technologies in the sub-6 GHz frequency range. These types of devices have shown strong potential for enabling high-performance miniaturized filters for future 5G front-ends.

TABLE I
PERFORMANCE COMPARISON OF THE STATE-OF-THE-ART

Mat. & mode	f (GHz)	k_t^2 (%)	Q	FoM	$f{\cdot}Q$
$LiTaO_3$ SAW [9]	2	7	1000	70	2.0×10^{12}
I.H.P SAW [10]	1.9	8	4000	320	7.6×10^{12}
I.H.P SAW [10]	3.5	8	1900	152	6.65×10^{12}
AlN FBAR [14]	2	4.7	3670	172	7.34×10^{12}
AlN FBAR [13]	5.1	6.4	913	58.4	4.56×10^{12}
Sc-AlN LVR [17]	0.53	4.5%	1240	56	0.66×10^{12}
$LiNbO_3$ LVR [24]	0.5	21.7%	1300	280	0.65×10^{12}
$LiNbO_3$ A1 [31]	4.35	29%	527	153	2.3×10^{12}
This work	**1.65**	**14%**	**3112**	**435**	$\mathbf{5.1\times10^{12}}$

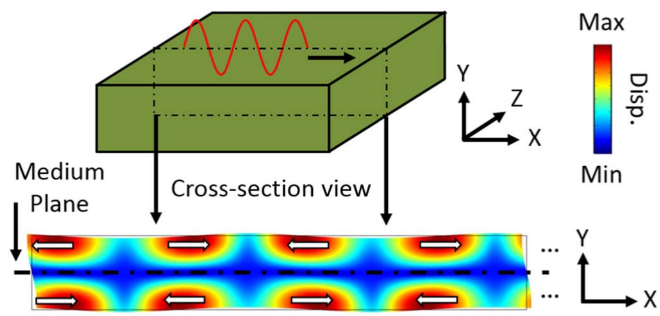

Fig. 1. Cross-sectional view of the displacement mode shape of the A1 mode propagating in a Y-cut $LiNbO_3$ slab. Y-cut LiNbO3 slab has mechanically free top and bottom surfaces and periodic boundaries in the lateral direction. The arrows denote the displacement directions.

II. THEORETICAL ANALYSIS AND MODELING

A. First-Order Antisymmetric (A1) Lamb Wave Mode

Antisymmetric Lamb wave modes are a class of Lamb-wave modes characterized by their particular anti-symmetry about the median plane of the plate. In other words, they have equal vertical displacement components but opposite longitudinal components on opposite sides of the median plane [34]. The order (n) of the antisymmetric Lamb wave modes is defined based on the relationship among cut-off frequency (f_c), wave velocity in the thickness direction (v_t), and the plate thickness (t) [34]:

$$f_c \times 2t = (2n - 1) \times v_t \quad (2)$$

So the first-order (n = 1) antisymmetric Lamb wave mode has a cut-off frequency equal to half the ratio between the wave velocity in the thickness direction and the plate thickness, and its Comsol-simulated eigenmode is shown in Fig. 1.

B. Design Parameters of A1

To more precisely predict the resonant frequency, we have to resort to a more refined model that treats the cross-section

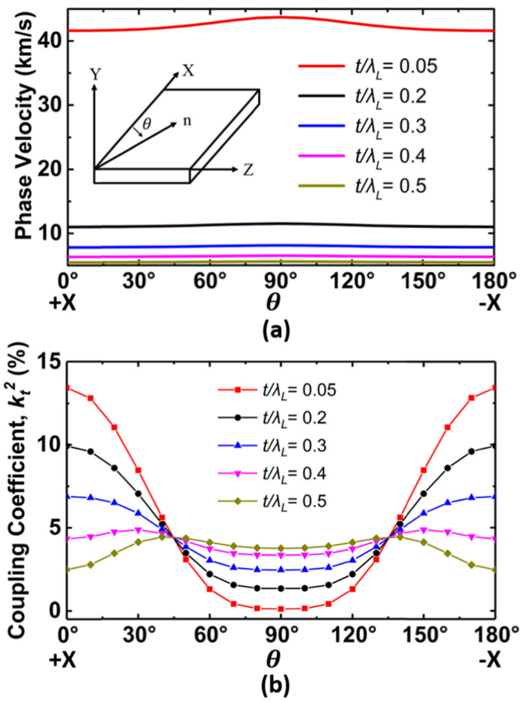

Fig. 2. Calculated (a) phase velocity and (b) electromechanical coupling coefficient (k_t^2) of the first-order antisymmetric (A1) Lamb-wave in a Y-cut $LiNbO_3$ thin film vs. the propagation direction for different ratios of film thickness to longitudinal wavelength (t/λ_L).

of the resonator as a two-dimensional cavity. The center frequency is then determined by the thickness of the thin film and the lateral dimensions of the motional cavity. The resonant frequency of A1 in a two-dimensional cavity with a thickness of t and width of G is given by

$$f_0 = \frac{v_L}{2t}\sqrt{\alpha^2 + (\frac{t}{G})^2} \tag{3}$$

where G is equal to half of the longitudinal wavelength ($\lambda_L/2$) and α is the ratio between the velocity of vertical and longitudinal directions:

$$\alpha = \sqrt{c_{55}/c_{11}} \tag{4}$$

where c_{11} and c_{55} are the stiffness constants [34].

Since $LiNbO_3$ is highly anisotropic, the device performance highly depends on the propagating orientations. To determine the optimal device orientation, the phase velocity of the A1 mode in Y-cut $LiNbO_3$ is first studied using COMSOL-based FEA. As shown in Fig. 2(a), the phase velocity is calculated as a function of the ratio between film thickness (t) and longitudinal wavelength (λ_L) with orientations varies from 0° to 180° to X-axis. The results suggest that the effect of orientations on phase velocity is small, and a smaller ratio of t/λ_L leads to a larger phase velocity. In addition to the phase velocity, the high electromechanical coupling coefficient (k_t^2) can be attained at the optimal device orientation and with a preferred ratio of t/λ_L. As shown in Fig. 2(b), as the orientation varies from 0° to 180° to +X axis in the Y-cut plane, k_t^2 changes with a maximum value along either the +X or -X-axis. Therefore, the devices in this work are all oriented

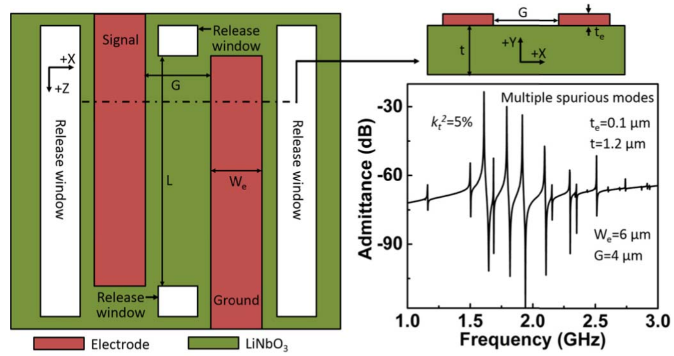

Fig. 3. Top and cross-section views of the Y-cut $LiNbO_3$ A1 mode resonator with FEA simulated response of an A1 mode resonator based on Y-cut $LiNbO_3$ (1.2 μm) with the conventional 2-electrode configuration.

along the +X axis. In addition to the device orientation, the ratio of t/λ_L also influences k_t^2 as Fig. 2(b) clearly shows that a lower t/λ_L produces a higher k_t^2.

In this work, we focus on the resonance around 1.7 GHz as the first step to understand and demonstrate the performance of A1 mode resonators using Y-cut $LiNbO_3$ thin films. Future work will focus on higher resonant frequencies. Based on the above analyses, we choose the thickness of the thin film to be 1.2 μm for the targeted resonant frequency.

C. Excitation and Spurious Modes

In addition to the resonant frequency, the transducer, which can excite A1 mode in the Y-cut $LiNbO_3$ thin film efficiently, needs to be considered based on the piezoelectric coupling matrix of $LiNbO_3$. Similar as the design in Z-cut $LiNbO_3$, A1 mode needs the electric field in the same direction of wave propagation. The simplest transducers for such a purpose are interdigital electrodes that are patterned exclusively on top of the $LiNbO_3$ thin film, which promises the least fabrication complication and low cost in manufacturing. As shown in Fig. 3, the 2 interdigital electrodes, when connected to signal and ground respectively, induce lateral alternating electric fields in the mechanically suspended $LiNbO_3$ thin film, which subsequently excite the resonator into A1 mode vibration. The design parameters of this 2-electrode resonator, labeled in Fig. 3, are listed in the inset. To attain maximum k_t^2, based on the analysis of optimal device orientation, the interdigital electrodes are paralleled with the Z-axis to excite lateral electric fields along the X-axis (Fig. 3). However, as shown in the Comsol-based FEA-simulated response (Fig. 3), the simulated k_t^2 is lower than the theoretical analysis and multiple unwanted spurious modes are excited near A1 mode. This is because the electric field excited by top interdigital electrodes within the thin film is non-uniform [35]–[37]. The non-uniform electric field introduces unwanted spurious modes, thus dispersing the transduction energy into various modes which lower the k_t^2 of the targeted mode.

To understand the origins of unwanted spurious modes, the non-uniform electric field is studied. As seen in Fig. 4 (a), the FEA-simulated distribution of electric field excited by top interdigital electrodes shows that the electric field can be

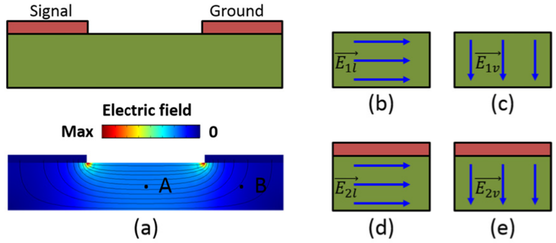

Fig. 4. (a) FEM-simulated result of electric field distribution with electric field lines. (b) Lateral and (c) vertical electric field in a section of the un-metalized $LiNbO_3$ thin film. (d) Lateral and (e) vertical electric field in a section of the metalized $LiNbO_3$ thin film.

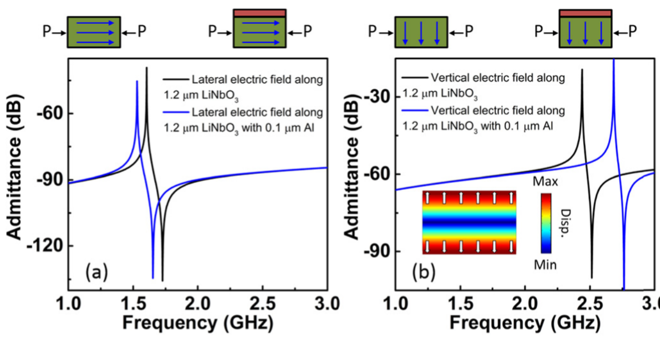

Fig. 5. Simulation structures with periodic boundaries and FEA-simulated results of the (a) A1 mode excited by the lateral electric field and (b) S1 mode excited by the vertical electric field in the sections of 1.2 μm $LiNbO_3$ thin film without and with 0.1 μm Al. The displacement mode shape of the S1 mode is included in the inset.

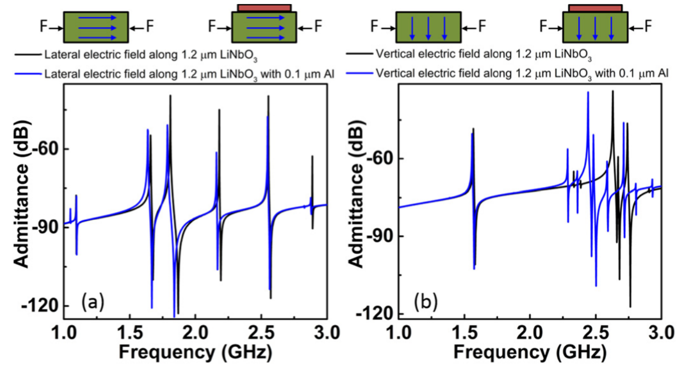

Fig. 6. Simulation structures with free boundaries and FEA-simulated results of the (a) A1 mode and spurious modes excited by the lateral electric field, and (b) S1 mode and spurious modes excited by the vertical electric field along 1.2 μm $LiNbO_3$ without and with 0.1 μm Al.

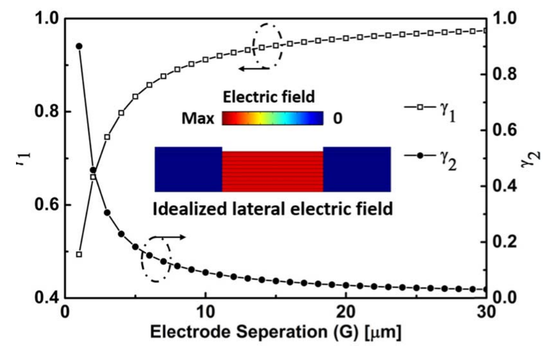

Fig. 7. Electric field strength ratios, γ_1 and γ_2, as functions of the electrode separation (G).

decomposed into lateral and vertical components in both the un-metalized (Point A) and metalized (Point B) sections of the $LiNbO_3$ thin films [Fig. 4(b)-(e)] [37]. To qualitatively understand the relationship between these E-field components and the spurious modes, idealized lateral and vertical electric fields are separately applied in the Y-cut $LiNbO_3$ thin films with periodic boundaries. As shown in Fig. 5 (a), one major unwanted spurious mode is the A1 sidetone excited by the lateral electric field in the section of the metalized $LiNbO_3$ thin film. This is because its resonant frequency is different from the targeted resonant frequency of the A1 mode which is excited by the lateral electric field in the section of the un-metalized $LiNbO_3$ thin film. The frequency difference is due to the change of equivalent stiffness and density after adding top electrodes [38]. As shown in Fig. 5 (b), other major unwanted spurious modes are the first-order symmetric modes (S1) excited by the vertical electric field in both the un-metalized and metalized sections of the $LiNbO_3$ thin film. The displacement mode shape of the S1 mode is shown in the inset of Fig. 5 (b).

In addition to the non-uniform electric field, the etched edges of the resonator body are another origin of the unwanted spurious modes. This is similar to SAW devices, these spurious modes are generated by the interference between desired waves and the reflected waves due to the mechanical free boundaries at the two lateral ends of the resonator body [39], [40]. As a comparison to the idealized situation, the periodic boundaries are replaced by free boundaries for the simulation in Fig. 6 to model the etched edges of the resonator body. Unlike the FEA-simulated results showed in Fig. 5, which has only one single mode for each structure, the admittance responses in Fig. 6 show the increased number of excited spurious modes and decreased value of k_t^2 of the targeted mode. To achieve the enhancement of k_t^2 and get rid of ripple responses of composed filters, these spurious modes need to be suppressed.

D. Suppression of Spurious Modes

Based on the above analysis, the spurious modes can be suppressed by optimizing the distribution of the electric field and decreasing the effect of the etched edges of the resonator body.

According to the simulation result in Fig. 4(a), the actual electric field has lateral and vertical components in the $LiNbO_3$ slab without and with top electrode [Fig. 4 (b)-(e)], and only the lateral electric field in $LiNbO_3$ slab without electrode (E_{1l}) contribute to the excitation of targeted A1 mode, while other components generate unwanted spurious modes. In the point of energy, the device transduction efficiency (k_t^2) in converting electrical energy to mechanical energy of different acoustic modes can be described by:

$$k_t^2 = \frac{U_{me}}{U_e + U_d} = \frac{\int T : d \cdot E dV}{\int T : s^E : T dV + \int E \cdot \varepsilon^T \cdot E dV} \quad (5)$$

where U_{me} is the mutual energy, U_e is the elastic energy, and U_d is the electric energy. T is the stress tensor, and E is the electric field. d, $s^{E,}$ and ε^T denote the piezoelectric strain constants, compliance constants at a constant electric field, and permittivity constants at constant stress respectively. For the A1 mode, its k_t^2 depends on the strength of effective lateral electric field (E_{1l}):

$$U_{meA1} = \int T : d \cdot E_{1l} dV \tag{6}$$

while the k_t^2 of spurious modes depends on the strength of E_{1v}, E_{2l}, and E_{2v} [Fig. 4 (c)-(e)].

To suppress the spurious modes caused by the non-uniform electric field, E_{1v}, E_{2l}, and E_{2v} should be decreased, and the simplest way is adjusting the electrode separation to optimize the electric field distribution. In our case, considering the limitation of lithography, the width of the electrodes is set to be 4 μm to simplify the analysis. To quantify the effect of electrode separation, the strength of the electric field in point A [Fig. 4(a)], where the center of the resonator body is, is compared to the strength of an idealized lateral electric field (E_{idea}) (as shown in the inset of Fig. 7) which is uniform and aligned in the lateral direction under the same potential:

$$\gamma_1 = |E_{1l}| \,/\, |E_{idea}| \tag{7}$$

Since E_{1l} and E_{idea} are excited under the same potential, the value of γ_1 indicates the degree of idealization and the optimized design should have γ_1 near equal to 1. To compare the strength of spurious modes and the targeted mode, the strength of E_{1v} at point A, E_{2l}, and E_{2v} at point B, where the center of the LiNbO3 cavity covered by electrodes, is compared to the strength of E_{1l}:

$$\gamma_2 = (|E_{1v}| + |E_{2l}| + |E_{2v}|) / |E_{1l}| \tag{8}$$

Based on the above analysis, the optimized design should have a maximum γ_1 and minimum γ_2. To find the relationships among γ_1, γ_2, and electrode separation, the width of the top electrodes is fixed with 4 μm in the FEA simulation considering the limitations of the lithography in the fabrication. As shown in Fig. 8, the data with electrode separation varied from 1 to 30 μm shows that increasing the electrode separation can increase γ_1 and decrease γ_2 simultaneously, suggesting a larger electrode separation for better spurious modes suppression. To further validate the analysis, the resonators with the structure shown in Fig. 4 are simulated for different electrode separations. As shown in Fig. 8, most significant spurious modes are mitigated through increasing the gap between interdigital electrodes from 4 μm [Fig. 8(a)] to 14 μm [Fig. 8(b)].

To suppress the spurious modes caused by the etched edges of the resonator body, we can borrow the idea from SAW devices that it is well known to apply acoustic absorbers or reflecting gratings between the IDT and the edges of the substrate to suppress the reflected acoustic waves [41]. In the view of energy, the proportion of reflected acoustic energy at the etched edges can be decreased to lower the proportion of the energy of spurious modes. To this end, multi pairs of interdigital electrodes are used to concentrate the acoustic energy in the lateral center of the resonator body. The $LiNbO_3$ sections without electrodes can be treated as high impedance sections, while the $LiNbO_3$ sections with electrodes can be treated as low impedance sections. As shown in Fig. 9, the whole resonator body can be modeled as the alternate connection of the high impedance sections and low impedance sections. The acoustic energy, transduced from electric energy by the interdigital electrodes, spreads in two lateral directions

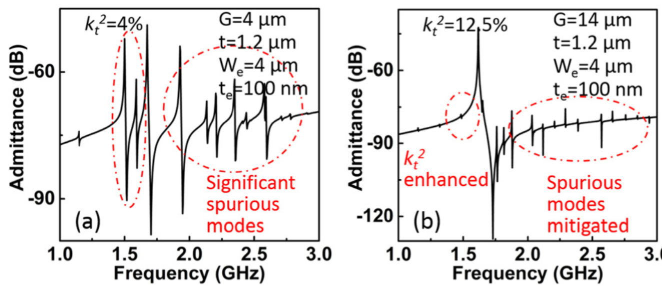

Fig. 8. FEA-simulated results of the devices with (a) G = 4 μm and (b) G = 14 μm.

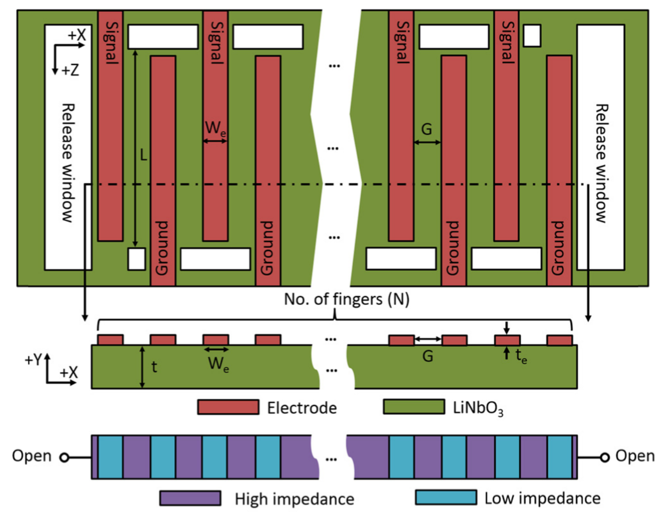

Fig. 9. Top and cross-section views of multi pairs of interdigital electrodes structure with the equivalent model of multi acoustic reflection sections.

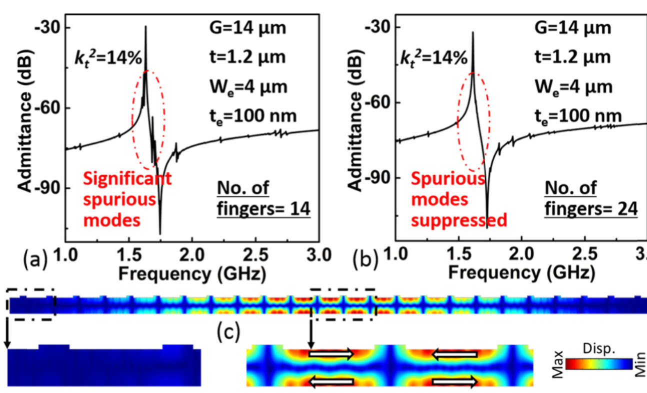

Fig. 10. FEA-simulated results of the devices with (a) N = 14 and (b) N = 24. (c) Displacement mode shape of A1 mode excited in (b) with the zoomed-in views in the center and edge of the resonator body.

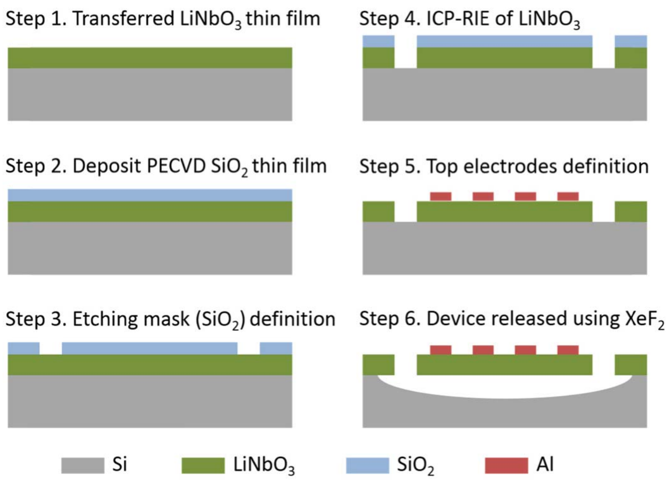

Fig. 11. Fabrication process for the Y-cut $LiNbO_3$ resonators.

from each high impedance section. As a result of reflection and transmission at each interface, the acoustic energy can be concentrated in the lateral center of the resonator body. Moreover, as the number of sections increases, the concentration of acoustic energy gradually becomes higher, and the proportion of reflected acoustic energy at edges becomes less. To validate the analysis of multi acoustic reflection sections, the resonators with different pairs of interdigital electrodes are simulated with 2D Comsol FEA. As shown in Fig. 10, most spurious modes can be suppressed by increasing the number of pairs to 24. The displacement mode shape of the device with 24 electrode fingers is shown in Fig. 10(c). The distribution of the amplitude of displacement confirms that the acoustic energy is concentrated in the lateral center of the resonator body. An optimal design is obtained with 24 electrodes and a 14 μm electrode gap under the consideration of performance and size.

III. Experimental Results and Discussions

A. Device Fabrication

To validate the analysis and modeling results, A1 resonators were fabricated with the process shown in Fig. 11. In the first step, a 1.2 μm thick Y-cut $LiNbO_3$ thin film was transferred onto a high resistivity Si wafer by NGK electronics. SiO_2 was then deposited via plasma-enhanced chemical vapor deposition (PECVD). In the third step, the PECVD SiO_2 was pattered with CHF_3-based reactive ion etching (RIE), serving as a hard mask for etching $LiNO_3$ thin film in step 4. To achieve high performance, the etching of $LiNbO_3$ was done by Cl_2-BCl_3-based RIE with inductively coupled plasma (ICP) to guarantee the straight etching profile. Afterward, the hard mask (SiO_2) is removed with HF, and 120 nm-thick Aluminum is subsequently defined as top electrodes on top of the $LiNbO_3$ thin film via a lift-off process. In the last step of the process, the Si under $LiNbO_3$ was removed with XeF_2-based dry etching to suspend the resonators.

The SEMs of different fabricated devices are shown in Fig. 12. As shown in Fig. 12(f), the etched sidewall, which serves as the acoustic boundary, has an angle of near 90°. According to previous work [42], straight acoustic boundaries lead to high-Q performance.

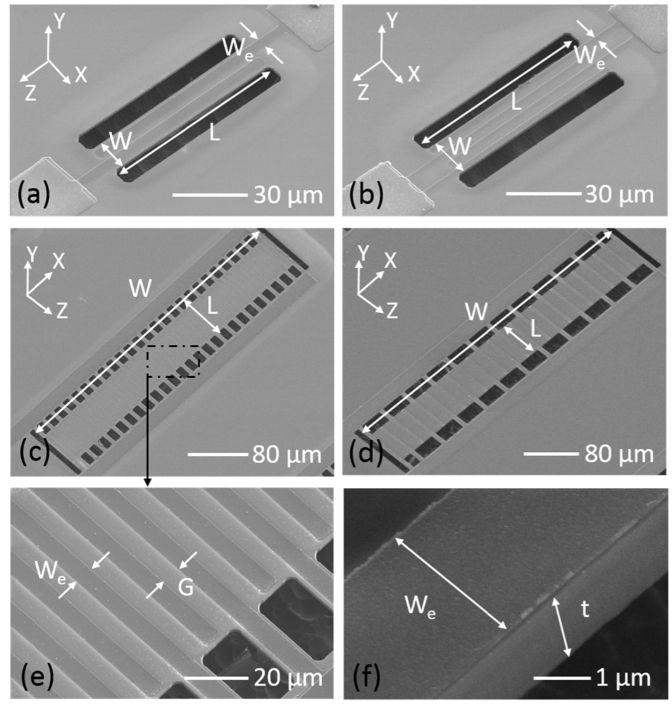

Fig. 12. SEM images of the (a) 2-electrode device, (b) 4-electrode device, (c) 52-electrode device, (d) 24-electrode device, (e) Zoomed-in view of multi-electrode device, and (f) sidewall of the etched $LiNbO_3$ thin film.

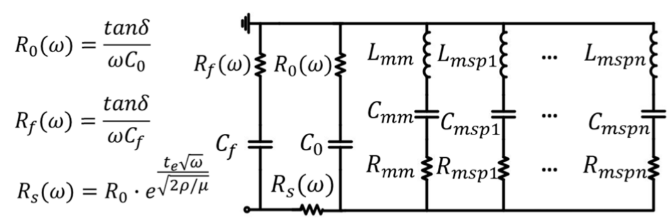

Fig. 13. Multi-resonance MBVD circuit model with multiple motional branches capturing the primary mode and spurious modes.

B. Extraction of Parameters

According to previous work, the effect of spurious modes should be accounted for in fitting to increase the accuracy of extraction [43]. A multi-resonance modified Butterworth-Van Dyke (MBVD) model, in which the resonances of main mode and significant spurious modes are captured by a motional branch of R_m, L_m, and C_m, is used to interpret the measurement results. As shown in Fig.13, the motional branch of the main mode is captured by R_{mm}, L_{mm}, and C_{mm}, while the motional branches of different spurious modes are captured by R_{mspn}, L_{mspn}, and C_{mspn}. The surface resistance of electrodes and leading lines are accounted for by adding resistor (R_s) in series, the value of which is depended on frequency due to the skin effect and calculated based on the equation shown in Fig. 13. To account for the parasitic effects, C_f and R_f

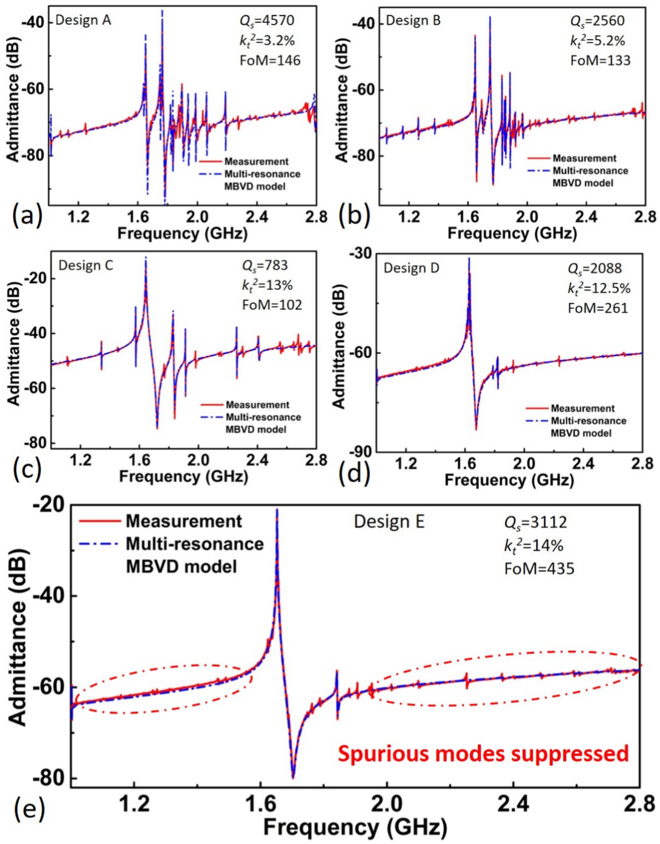

Fig. 14. Measurement results of various designs: (a) A, (b) B, (c) C, (d) D, and (e) E. The parameters and measured key values of these designs are listed in Table II.

are included as the feedthrough capacitance and loss in the substrate ($tan\delta$), respectively.

C. Measured Admittance Responses

The fabricated devices were characterized at room temperature with a Keysight N5249A PNA network analyzer. The measured admittance responses of 5 different designs are shown in Fig. 14. Excellent agreement has been reached between the theoretical analysis and measurements. As shown in Fig. 14(a), the design A with two electrodes and a gap of 4 μm shows k_t^2 of only 3%, which is far below the theoretical value [Fig. 2(b)] due to the dispersing of energy into various modes. To attenuate the acoustic energy of reflection-producing spurious modes, multiple electrodes are used in design B and C. The design B [Fig. 14(b)] with 4 electrodes shows k_t^2 of 5.2% and the design C [Fig. 14(c)] with 52 electrodes shows k_t^2 of 13%. The increasing of k_t^2 indicates the attenuation of spurious modes, while there are still some significant spurious in the admittance response of design C due to the non-uniform electric field. The electrodes separation of 14 μm is used in the design D and E to make the electric field, excited by top electrodes, close to the idealized lateral electric field. The difference between design D and E is the number of electrodes. The design D with 14 electrodes shows k_t^2 of 12.5%, and the design E with 24 electrodes, which exhibit notably suppression of spurious modes, shows k_t^2 of 14%. In addition to the spurious mode suppression, the Q_s also gets enhanced up to 3112 in the optimized design E [Fig. 14(e)].

TABLE II
DESIGN PARAMETERS AND MEASURED KEY VALUES OF THE FABRICATED A1 DEVICES

Design	A	B	C	D	**E**
W (µm)	18	32	424	242	422
N	2	4	52	14	24
G (µm)	4	4	4	14	14
W_e (µm)	6	4	4	4	4
L (µm)	80	80	80	80	80
t (µm)	1.2	1.2	1.2	1.2	1.2
t_e (nm)	100	100	100	100	100
$R_m + R_s$ (Ω)	63	74	4	35	11
f_0 (GHz)	1.75	1.75	1.65	1.65	**1.65**
k_t^2	3%	5.2%	13%	12.5%	**14%**
Q_s	4570	2560	783	2088	**3112**
FoM	146	133	102	261	**435**

Based on the comparison of all these five designs, by employing wider gaps (larger γ_1 and smaller γ_2) and multi-pairs of electrodes, all significant spurious modes are suppressed, and the FoM is notably enhanced. Parameters and measured key values of these five different designs are listed in Table II.

IV. CONCLUSION

In this work, A1 mode $LiNbO_3$ MEMS resonators have been presented and the optimized design has been demonstrated at 1.65 GHz with an FoM as high as 435, an $f \cdot Q$ product of 5.1×10^{12} Hz and a near spurious-free response. Different configurations of electrodes have also been explored for achieving high FoMs and spurious-free response. The A1 Y-cut $LiNbO_3$ MEMS resonators have shown strong potential for enabling higher performance filters for next-generation RF front-ends.

REFERENCES

[1] *Before the Federal Communications Commission*, Federal Commun. Commission, Washington, DC, USA, 2009.
[2] Y. Yang, R. Lu, and S. Gong, “A 1.65 GHz lithium niobate A1 resonator with electromechanical coupling of 14% and Q of 3112,” in *Proc. IEEE 32nd Int. Conf. Micro Electro Mech. Syst. (MEMS)*, Jan. 2019, pp. 875–878.
[3] Y. Yang, R. Lu, T. Manzaneque, and S. Gong, “1.7 GHz Y-cut lithium niobate MEMS resonators with FoM of 336 and fQ of 9.15×10^12,” in *IEEE MTT-S Int. Microw. Symp. Dig.*, Jun. 2018, pp. 563–566.
[4] *5G New Radio Solutions: Revolutionary Applications Here Sooner Than You Think*, Skyworks Solutions, San Irvine, CA, USA. Accessed: Nov. 5, 2019. [Online]. Available: https://www.skyworksinc.com
[5] *Spectrum for 4G and 5G*, Qualcomm Technol., San Diego, CA, USA, 2017. [Online]. Available: https://www.qualcomm.com/media/documents/spectrum-4g-and-5g
[6] T. Nakamura, “Proposal for candidate radio interface technologies for IMT-advanced based on LTE release 10 and beyond Takehiro Nakamura,” in *Proc. ITU-R WP 5D 3rd Work. IMT-Adv.*, 2009, pp. 17–18.

[7] *Bandwidth Support in LTE Standards*, Qualcomm Technol., San Diego, CA, USA, 2012. [Online]. Available: https://transition.fcc.gov/bureaus/oet/tac/tacdocs/meeting71612/PANEL2.3-Gaal-Qualcomm.pdf

[8] H. Bhugra and G. Piazza, *Piezoelectric MEMS Resonators*. Cham, Switzerland: Springer, 2017.

[9] T. Kimura, M. Kadota, and Y. Ida, "High Q SAW resonator using upper-electrodes on grooved-electrodes in LiTaO3," in *IEEE MTT-S Int. Microw. Symp. Dig.*, May 2010, pp. 1740–1743.

[10] T. Takai *et al.*, "I.H.P. SAW technology and its application to microacoustic components (Invited)," in *Proc. IEEE Int. Ultrason. Symp. (IUS)*, Sep. 2017, pp. 1–8.

[11] T. Kimura, M. Omura, Y. Kishimoto, and K. Hashimoto, "Applicability investigation of SAW devices in the 3 to 5 GHz range," in *IEEE MTT-S Int. Microw. Symp. Dig.*, Jun. 2018, pp. 846–848.

[12] T. Kimura, M. Omura, Y. Kishimoto, and K. Hashimoto, "Comparative study of acoustic wave devices using thin piezoelectric plates in the 3–5-GHz range," *IEEE Trans. Microw. Theory Techn.*, vol. 67, no. 3, pp. 915–921, Mar. 2019.

[13] Y. Satoh, T. Nishihara, T. Yokoyama, M. Iwaki, and T. Miyashita, "Development of 5 GHz FBAR filters for wireless systems," in *Proc. Int. Symp. Acoust. Wave Device Future Mob. Commun. Syst.*, Feb. 2015, pp. 5–8.

[14] R. Ruby, R. Parker, and D. Feld, "Method of extracting unloaded Q applied across different resonator technologies," in *Proc. IEEE Ultrason. Symp.*, Nov. 2008, pp. 1815–1818.

[15] R. Ruby *et al.*, "Positioning FBAR technology in the frequency and timing domain," *IEEE Trans. Ultrason., Ferroelectr., Freq. Control*, vol. 59, no. 3, pp. 334–345, Mar. 2012.

[16] M. Akiyama, T. Kamohara, K. Kano, A. Teshigahara, Y. Takeuchi, and N. Kawahara, "Enhancement of piezoelectric response in scandium aluminum nitride alloy thin films prepared by dual reactive cosputtering," *Adv. Mater.*, vol. 21, no. 5, pp. 593–596, Feb. 2009.

[17] L. Colombo, A. Kochhar, C. Xu, G. Piazza, S. Mishin, and Y. Oshmyansky, "Investigation of 20% Scandium-doped Aluminum Nitride films for MEMS laterally vibrating resonators," in *Proc. IEEE Int. Ultrason. Symp. (IUS)*, Sep. 2017, pp. 1–4.

[18] M. D. Henry, T. R. Young, E. A. Douglas, and B. A. Griffin, "Reactive sputter deposition of piezoelectric $Sc_{0.12}Al_{0.88}$ N for contour mode resonators," *J. Vac. Sci. Technol. B*, vol. 36, no. 3, 2018, Art. no. 03E104.

[19] R. Aigner, G. Fattinger, M. Schaefer, K. Karnati, R. Rothemund, and F. Dumont, "BAW filters for 5G bands," in *IEDM Tech. Dig.*, Dec. 2018, pp. 14.5.1–14.5.4.

[20] D. Psychogiou, R. Gomez-Garcia, R. Loeches-Sanchez, and D. Peroulis, "Hybrid acoustic-wave-lumped-element resonators (AWLRs) for high-*Q* bandpass filters with quasi-elliptic frequency response," *IEEE Trans. Microw. Theory Techn.*, vol. 63, no. 7, pp. 2233–2244, Jul. 2015.

[21] X. Lu, K. Mouthaan, and Y. T. Soon, "Wideband bandpass filters with SAW-filter-like selectivity using chip SAW resonators," *IEEE Trans. Microw. Theory Techn.*, vol. 62, no. 1, pp. 28–36, Jan. 2014.

[22] C. Zuo, C. He, W. Cheng, and Z. Wang, "Hybrid filter design for 5G using IPD and acoustic technologies," in *Proc. IEEE Int. Ultrason. Symp.*, Oct. 2019, pp. 1–4.

[23] S. Gong and G. Piazza, "Design and analysis of lithium-niobate-based high electromechanical coupling RF-MEMS resonators for wideband filtering," *IEEE Trans. Microw. Theory Techn.*, vol. 61, no. 1, pp. 403–414, Dec. 2013.

[24] S. Gong and G. Piazza, "Figure-of-merit enhancement for laterally vibrating lithium niobate MEMS resonators," *IEEE Trans. Electron Devices*, vol. 60, no. 11, pp. 3888–3894, Nov. 2013.

[25] S. Gong, Y.-H. Song, T. Manzaneque, R. Lu, Y. Yang, and A. Kourani, "Lithium niobate MEMS devices and subsystems for radio frequency signal processing," in *Proc. IEEE 60th Int. Midwest Symp. Circuits Syst. (MWSCAS)*, Aug. 2017, pp. 45–48.

[26] R. H. Olsson *et al.*, "A high electromechanical coupling coefficient SH0 Lamb wave lithium niobate micromechanical resonator and a method for fabrication," *Sens. Actuators A, Phys.*, vol. 209, pp. 183–190, Mar. 2014.

[27] R. Wang, S. A. Bhave, and K. Bhattacharjee, "Design and fabrication of S0 Lamb-wave thin-film lithium niobate micromechanical resonators," *J. Microelectromech. Syst.*, vol. 24, no. 2, pp. 300–308, Apr. 2015.

[28] M. Pijolat *et al.*, "Large electromechanical coupling factor film bulk acoustic resonator with X-cut LiNbO3 layer transfer," *Appl. Phys. Lett.*, vol. 95, no. 18, Nov. 2009, Art. no. 182106.

[29] M. Gorisse *et al.*, "High frequency $LiNbO_3$ bulk wave resonator," in *Proc. Joint Conf. IEEE Int. Freq. Control Symp. Eur. Freq. Time Forum (EFTF/IFC)*, Apr. 2019, pp. 1–2.

[30] M. Kadota, T. Ogami, K. Yamamoto, and H. Tochishita, "$LiNbO_3$ thin film for A1 mode of Lamb wave resonators," *Phys. Status Solidi A*, vol. 208, no. 5, pp. 1068–1071, May 2011.

[31] Y. Yang, A. Gao, R. Lu, and S. Gong, "5 Ghz lithium niobate MEMS resonators with high FoM of 153," in *Proc. IEEE 30th Int. Conf. Micro Electro Mech. Syst. (MEMS)*, Jan. 2017, pp. 942–945.

[32] Y. Yang, R. Lu, T. Manzaneque, and S. Gong, "Toward Ka band acoustics: Lithium niobate asymmetrical mode piezoelectric MEMS resonators," in *Proc. IEEE Int. Freq. Control Symp. (IFCS)*, May 2018, pp. 1–5.

[33] V. Plessky, S. Yandrapalli, P. Turner, L. Villanueva, J. Koskela, and R. Hammond, "5 GHz laterally-excited bulk-wave resonators (XBARs) based on thin platelets of lithium niobate," *Electron. Lett.*, vol. 55, no. 2, pp. 98–100, Jan. 2019.

[34] D. Royer, D. P. Morgan, and E. Dieulesaint, *Elastic Waves in Solids I: Free and Guided Propagation*. Berlin, Germany: Springer, 2000.

[35] D. J. Warkentin, "Modeling and electrode optimization for torsional IDE piezoceramics," in *Proc. Smart Struct. Mater., Smart Struct. Integr. Syst.*, vol. 3985, Jun. 2000, pp. 840–855.

[36] C. R. Bowen, L. J. Nelson, R. Stevens, M. G. Cain, and M. Stewart, "Optimisation of interdigitated electrodes for piezoelectric actuators and active fibre composites," *J. Electroceram.*, vol. 16, no. 4, pp. 263–269, Jul. 2006.

[37] W. Smith, H. Gerard, J. Collins, T. Reeder, and H. Shaw, "Analysis of interdigital surface wave transducers by use of an equivalent circuit model," *IEEE Trans. Microw. Theory Techn.*, vol. MTT-17, no. 11, pp. 856–864, Nov. 1969.

[38] R. Lu, Y. Yang, M.-H. Li, M. Breen, and S. Gong, "5-GHz antisymmetric mode acoustic delay lines in lithium niobate thin film," *IEEE Trans. Microw. Theory Techn.*, to be published.

[39] R. S. Wagers, "Spurious acoustic responses in SAW devices," *Proc. IEEE*, vol. 64, no. 5, pp. 699–702, May 1976.

[40] M. Suthers, G. Este, R. Streater, and B. MacLaurin, "Suppression of spurious SAW signals," in *Proc. IEEE Ultrason. Symp.*, Nov. 1986, pp. 37–42.

[41] M. Suthers, G. Este, R. Streater, and B. MacLaurin, "Saw devices with reflection-suppressing fingers," U.S. Patent 4 642 507, Feb. 10, 1987.

[42] Y.-H. Song, R. Lu, and S. Gong, "Analysis and removal of spurious response in SH0 lithium niobate MEMS resonators," *IEEE Trans. Electron Devices*, vol. 63, no. 5, pp. 2066–2073, May 2016.

[43] R. Lu, M.-H. Li, Y. Yang, T. Manzaneque, and S. Gong, "Accurate extraction of large electromechanical coupling in piezoelectric MEMS resonators," *J. Microelectromech. Syst.*, vol. 28, no. 2, pp. 209–218, Apr. 2019.

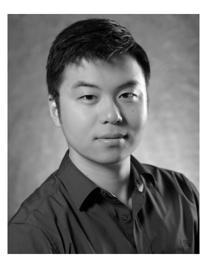

Yansong Yang (Member, IEEE) received the B.S. degree in electrical and electronic engineering from the Huazhong University of Science and Technology, Wuhan, China, in 2014, and the M.S. and Ph.D. degrees in electrical engineering from the University of Illinois at Urbana–Champaign, Urbana, IL, USA, in 2017 and 2019, respectively. He is currently a Postdoctoral Researcher with the University of Illinois at Urbana–Champaign. His research interests include design and microfabrication techniques of RF MEMS resonators, filters, switches, and photonic integrated circuits. He has received the 2nd Place in Best Paper Competition at the 2018 IEEE International Microwave Symposium, the Best Paper Award at 2019 IEEE International Ultrasonics Symposium, and the 2019 P. D. Coleman Graduate Research Award from the Department of Electrical and Computer Engineering, UIUC. He was also a finalist for the Best Paper Award at the 2018 IEEE International Frequency Control Symposium.

Ruochen Lu (Member, IEEE) received the B.E. degree (Hons.) in microelectronics from Tsinghua University, Beijing, China, in 2014, and the M.S. and Ph.D. degrees in electrical engineering from the University of Illinois at Urbana–Champaign, Urbana, IL, USA, in 2017 and 2019, respectively. He is currently a Postdoctoral Researcher with the University of Illinois at Urbana–Champaign. His research interests include radio frequency microsystems and their applications for timing and signal processing. He received the Best Student Paper Awards at the 2017 IEEE International Frequency Control Symposium and the 2018 IEEE International Ultrasonics Symposium. He was also a recipient of the 2015 Lam Graduate Award from the College of Engineering, UIUC, the 2017 Nick Holonyak, Jr. Graduate Research Award, the 2018 Nick Holonyak, Jr. Fellowship, and the 2019 Raj Mittra Outstanding Research Award from the Department of Electrical and Computer Engineering, UIUC.

Songbin Gong (Senior Member, IEEE) received the Ph.D. degree in electrical engineering from the University of Virginia, Charlottesville, VA, USA, in 2010. He is currently an Associate Professor and the Intel Alumni Fellow with the Department of Electrical and Computer Engineering and the Micro and Nanotechnology Laboratory, University of Illinois at Urbana–Champaign, Urbana, IL, USA. His research primarily focuses on design and implementation of radio frequency microsystems, components, and subsystems for reconfigurable RF front ends. In addition, his research explores hybrid microsystems based on the integration of MEMS devices with photonics or circuits for signal processing and sensing. He is a Technical Committee member of MTT-21 RF-MEMS of the IEEE Microwave Theory and Techniques Society, International Frequency Control Symposium, and International Electron Devices Meeting. He was a recipient of the 2014 Defense Advanced Research Projects Agency Young Faculty Award, the 2017 NASA Early Career Faculty Award, the 2019 UIUC College of Engineer Dean's Award for Excellence in Research, and the 2019 Ultrasonics Early Career Investigator Award. Along with his students and postdocs, he received the Best Paper Awards from the 2017 and 2019 IEEE International Frequency Control Symposium, the 2018 and 2019 International Ultrasonics Symposium, and awarded 2nd Place in Best Paper Competition at the 2018 IEEE International Microwave Symposium. He currently serves as the Chair of MTT TC2 and TC 21, and an Associate Editor for T-UFFC and JMEMS.